Dalton Transactions

ROYAL SOCIETY OF CHEMISTRY

PAPER

View Article Online
View Journal | View Issue

Cite this: *Dalton Trans.*, 2026, **55**, 4821

NO photoswitches: a single photoinduced linkage isomer in diamagnetic {MNO}^{8} complexes

Artem A. Mikhailov, [a] Axel Gansmüller, [a] Asma Hasil,[a,b] Sébastien Pillet,[a] Gennadiy Kostin, [c] Guillaume Chastanet, [d] Theo Woike[a] and Dominik Schaniel *[a]

Representative for the {MNO}^{8} series of metal-nitrosyl compounds, the neutral {CoNO}^{8} cobalt nitrosyl complex [Co(fpin)NO(phen)] (**1**) with fpin = perfluoropinacolate($^{2-}$) and phen = phenanthroline(^{0}) exhibits a single photoinduced linkage isomer (PLI) that can be generated by irradiation with red light. The high population of 80% PLI enables the unambiguous determination of its structure as a bent κO isonitrosyl Co–O–N with a Co–O–N angle of 123.1(3)° compared to the bent κN nitrosyl Co–N–O ground state with an angle of 121.199(14)°. While the photoswitching in this diamagnetic {CoNO}^{8} complex is triggered by a metal-to-ligand charge transfer transition like in the well-known {MNO}^{6} complexes, the vibrational response is opposite, yielding a blue-shift of the N–O stretching vibration upon isonitrosyl PLI generation in {MNO}^{8} and a red-shift in {MNO}^{6}. First-principles DFT calculations, performed on the photocrystallography models, provide results consistent with the observed structures and vibrational spectra. Additionally, the analysis of the Bader charges shows that the charge on the NO is more positive in the PLI compared to the GS for both the {MNO}^{8} and {MNO}^{6} complexes. Hence, the experimental vibrational spectra should not be directly used as sole evidence to derive underlying structures or electron density changes.

Received 16th January 2026,
Accepted 17th February 2026

DOI: 10.1039/d6dt00116e

rsc.li/dalton

Introduction

Irradiation of transition metal nitrosyl complexes with light can lead either to NO release, a phenomenon of interest for medical applications such as photodynamic or photothermal therapy,[1–3] or the generation of photoinduced linkage isomers (PLIs) of the nitrosyl ligand, which might be used in optical applications due to the significant photochromic and photorefractive effects.[4–6] These two phenomena might compete, especially during the first steps of the photoinduced reaction,[7,8] and it is thus of importance to study these ultrafast processes with appropriate methods. Time resolved infrared spectroscopy (TRIR) is an excellent method for the identification of transient and intermediate reactive molecular species,[9] and it has already been applied to study the formation of PLIs of the NO ligand in $Na_2[Fe(CN)_5NO]$ (SNP).[10,11] However, the attribution of a detected vibrational band to a specific type of linkage isomer is non-trivial, since the NO might adopt a variety of geometrical configurations. Hence, the interpretation relies on static spectroscopic measurements, which together with X-ray diffraction studies under light irradiation establish the boundary structures of the initial ground state (GS) and the final metastable PLI, which can be trapped at low temperatures.[12] This type of approach is well established for metal-nitrosyl complexes of the {MNO}^{6} series (using the Enemark–Feltham notation, the superscript gives the number of metal d electrons, considering the nitrosyl ligand as NO^+), where two types of PLI, an isonitrosyl (MS1, κO) and a side-on (MS2, κ^2N,O) configuration of the NO ligand, have been described for a large number of complexes.[13–15] Typically, compared to the GS, the NO stretching frequency shifts by 100–150 and 300–350 cm^{-1} to lower wavenumbers for MS1 and MS2, respectively. We have recently shown on the example of $K_2[RuCl_5NO]$ that care has to be taken if one wants to extract further information such as the oxidation state (OS) or the charge on the NO ligand from vibrational spectroscopy, since the vibrations of the involved groups are strongly coupled and the coupling changes during the formation of PLIs.[16]

For the {MNO}^{8} series, there is much less experimental evidence of NO PLI, the first example being {PtNO}^{8} where infrared spectroscopy showed a shift of the NO stretching vibration to higher wavenumbers upon the formation of one PLI.[17,18]

[a]*Université de Lorraine, CNRS, CRM2, 5400 Nancy, France. E-mail: dominik.schaniel@univ-lorraine.fr*
[b]*Mines St Etienne, Ctr SPIN, UMR CNRS 5307, LGF, 42023 St Etienne, France*
[c]*Nikolaev Institute of Inorganic Chemistry, Siberian Branch of the Russian Academy of Sciences, 3 Acad. Lavrentiev Avenue, Novosibirsk 630090, Russian Federation*
[d]*Univ. Bordeaux, CNRS, Bordeaux INP, ICMCB, UMR 5026, F-33600 Pessac, France*

Although no experimental structure of the PLI could be measured, DFT calculations showed that both in the GS and in the PLI, the NO ligand is bent, adopting a N-bound configuration in the GS and an O-bound configuration in the PLI. The second example concerns $\{RhNO\}^8$ where infrared spectroscopy again showed a shift of the NO stretching frequency to higher wavenumbers, and the photocrystallographic measurements indicated an increase in the Rh–N–O angle from 125° to 161° but were not conclusive on whether the PLI is an isonitrosyl or a nitrosyl configuration.[19] The $\{MNO\}^8$ situation is interesting as it differs significantly from the $\{MNO\}^6$ situation due to the additional 2 electrons that occupy orbitals of the d(z^2) and/or d($x^2 - y^2$) type, which can either result in a diamagnetic or a paramagnetic complex. $\{CoNO\}^8$ complexes have been studied extensively, and the two Co → NO backbonds can result with d(xz)/d(yz) in a linear Co–N–O configuration, or with d(z^2)/d(yz) in a bent configuration.[20,21] Despite extensive research on the electronic ground state of $\{CoNO\}^8$, there is no PLI reported for this class of compounds. There is one study on a $\{CoNO\}^{10}$ complex with a linear configuration in the GS, $[Co(CO)_3(NO)]$,[22] for which through TRIR combined with DFT the photo-excited state has been ascribed to a bent triplet state (Co–N–O angle of the order of 155–167°) which relaxes within 350 ps to a relatively stable minimum (>1 ns, lifetime not measured) with a Co–N–O angle of 137°. This study points to another important question in the $\{CoNO\}^8$ family, *i.e.*, whether the linear and bent configurations systematically correspond to triplet or singlet states and whether one can switch between these two structural configurations. Using two-dimensional infrared spectroscopy, Marroux *et al.*[23] reported an ultrafast structural interconversion between the linear and bent configurations in $[CoCl_2(NO)(PMePh_2)_2]$. The interconversion between the linear singlet isomer and the bent triplet isomer occurs on the picosecond time scale at room temperature in thermal equilibrium in solution. Concerning photoinduced NO release, a recent study on a $\{CoNO\}^8$ complex demonstrated the photolysis under white light irradiation in aqueous solution.[24] Harrop and co-workers[25,26] showed that $\{CoNO\}^8$ complexes can serve as HNO donors under reaction with H^+.

In order to investigate the properties as well as the conditions for the generation of the PLI in the $\{CoNO\}^8$ series, we studied in detail the complex [Co(fpin)NO(phen)] (**1**). We first describe the structures of the GS and PLI obtained from X-ray diffraction (XRD) and supported by DFT calculations. Second, we discuss the photogeneration mechanism and the electronic and magnetic properties based on UV-Vis spectroscopy, X-ray absorption spectroscopy and magnetic measurements under *in situ* light irradiation. Third, we analyse in detail the experimental vibrational spectra and compare them with DFT calculations, performed on the periodic crystalline systems, to obtain the force constants and the decoupled modes using the Cremer–Kraka formalism.[27]

Results

Structure of GS and PLI

In their recent work, Popp *et al.*[20] showed that the penta-coordinated $\{CoNO\}^8$ complex [Co(fpin)NO(phen)] (**1**) with fpin = perfluoropinacolate($^{2-}$) and phen = phenanthroline(^{0}) with a bent NO is formally a diamagnetic $\{Co(I)NO^+\}$ with $3d^8$ d-orbital population. We performed X-ray diffraction (XRD) on the single crystals of (**1**) at 5 K under light irradiation. In the GS, the complex crystallises in the triclinic space group $P\bar{1}$ with cell parameters: a = 8.4918(4) Å, b = 8.7777(4) Å, c = 13.2804(6) Å, α = 94.784(4)°, β = 90.250(4)°, and γ = 93.681(4)° and with two molecules per unit cell (Z = 2). The molecular

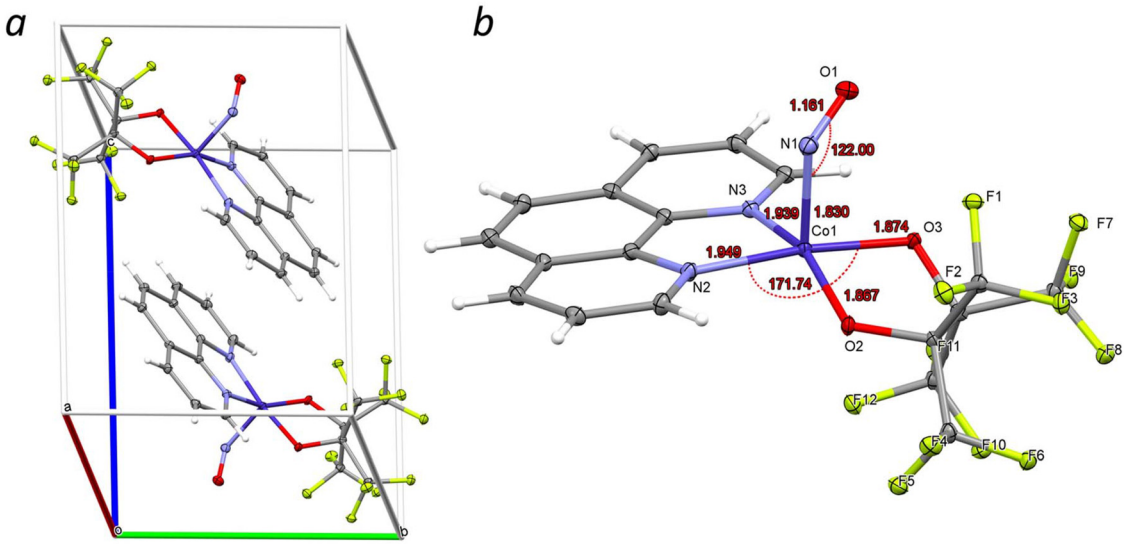

Fig. 1 (a) Unit cell showing the arrangement of the two molecules related by an inversion center; (b) details of the molecular structure indicating selected distances [Å] and angles [°] around the central penta-coordinated Co metal atom.

Table 1 The most relevant measured and calculated (DFT on periodic crystalline systems) atomic distances and angles of GS and PLI and their differences

	GS_{exp}	PLI_{exp}	GS_{DFT}	PLI_{DFT}	$\Delta(PLI-GS)_{exp}$	$\Delta(PLI-GS)_{DFT}$	Δ(DFT–Exp) GS/PLI
Bond length (Å)							
Co1–N1	1.8299(17)	1.986(5)	1.7608	1.8859	+0.156	+0.1251	−0.0691
Co1–O1A							−0.100
Co1–O1	2.636(1)	2.796(6)	2.6171	2.7506	+0.160	+0.1335	−0.0189
Co–N1A							−0.045
N1–O1	1.161(2)	1.163(5)	1.1822	1.1708	+0.002	−0.0114	+0.021
O1A–N1A							+0.008
Co1–O2	1.8666(13)	1.867(2)	1.8391	1.8349	+0.000	−0.0042	−0.0275/−0.032
Co1–O3	1.8736(13)	1.874(2)	1.8571	1.8533	+0.0004	−0.0038	−0.0165/−0.021
Co1–N2	1.9488(16)	1.941(2)	1.9061	1.8794	−0.0078	−0.0267	−0.0427/−0.062
Co1–N3	1.9388(16)	1.938(2)	1.8820	1.8779	−0.0008	−0.0041	−0.0568/−0.060
Angle (°)							
Co1–N1–O1	121.99(14)	123.1(3)	124.38	126.69	+1.14	+2.31	+2.39
Co1–O1A–N1A							+3.59
N2–Co1–O3	171.74(7)	174.32(11)	172.73	175.7	+2.58	+2.98	+0.99/+1.39
N3–Co1–O2	158.57(7)	163.74(10)	148.36	159.59	+5.17	+11.23	−10.21/−4.15

arrangement in the unit cell and the first coordination sphere of the central cobalt atom with atomic distances and angles are presented in Fig. 1a and b, respectively, and further structural details are given in Table 1. The coordination polyhedron of the cobalt central atom is close to a square pyramid with NO in the axial position and the oxygen atoms O3 and O2 of fpin and the nitrogen atoms N2 and N3 of phen forming the basal plane. We note two characteristic features of the molecular structure: a bent Co1–N1–O1 with an angle of 122.99 (14)° and a displacement of the Co1 out of the basal plane towards the NO group, resulting in angles of N2–Co1–O3 = 171.74(7)° and N3–Co1–O2 = 158.57(7)° and distances of Co1–O2 = 1.8666(13) Å, Co1–O3 = 1.8736(13) Å, Co1–N2 = 1.9488(16) Å, and Co1–N3 = 1.9388(16) Å. Overall, the basal plane is a slightly distorted square and Co1 is 0.3537 Å above the N3–O2 basal line and 0.1344 Å above the N2–O3 basal line. Concerning the crystalline packing, due to the neutrality of the complex, the bonding forces of the crystal are van der Waals-like. The shortest intramolecular contacts of the oxygen O1 of the N1O1 ligand are an oxygen of the fpin at O1–O3 = 2.813(2) Å, which is closer than the nitrogen atom of the phen at O1–N3 = 3.124(2) Å. The three shortest intermolecular contacts are with three different neighbouring molecules, the shortest is with a hydrogen atom at O1–H15 = 2.725 Å, followed by two contacts with fluorine atoms at O1–F1 = 2.984(2) Å and at O1–F8 = 2.984(2) Å. Hence, there is enough space available for the NO rotation in view of PLI generation.

As will be shown below, the decay of the PLI efficiently occurs at $T > 50$ K or by exposure to infrared light. Therefore, in order to avoid any thermally or light-induced depopulation of the PLI, we have continuously irradiated the sample with light of $\lambda = 590$ nm during XRD data collection at $T = 5$ K. In this manner, we obtained a high population of the PLI of 76 (2)% in agreement with the results of infrared spectroscopy. The details of the refinement are given in the SI (Table S1). The best model for the PLI is obtained from a fit with a disordered model with two NO ligands, a Co–N–O for the GS and a Co–O–N for the PLI with refined occupancies of 0.24(2) and 0.76(2), respectively. Fig. 2a shows an overlay of the GS and PLI structures, illustrating the elongation of Co–O (with respect to Co–N) and the movement of Co towards the basal plane. Details of the molecular structure of the PLI are shown in Fig. 2b and will be discussed below in comparison to the results obtained by subsequent DFT structure optimization. The quality of the model has been checked by inspection of the residual density maps (Fig. 3). The residual electron

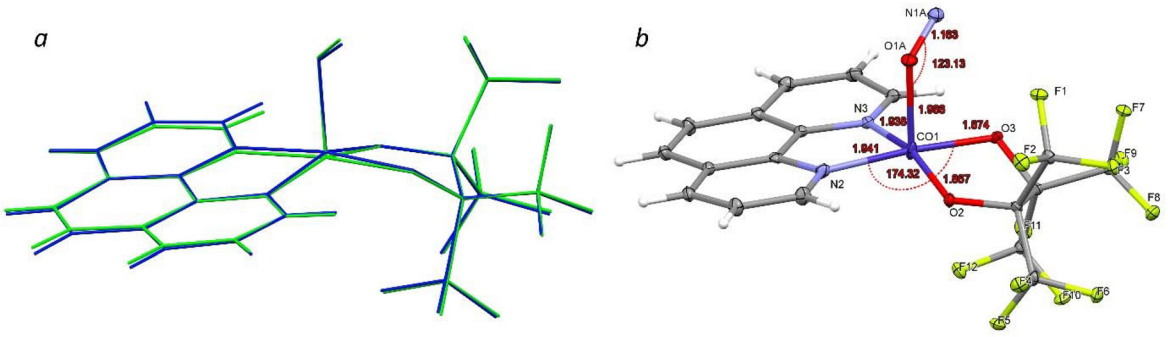

Fig. 2 (a) Overlay of the GS (blue) and the PLI (green); (b) structure of the PLI with chosen distances [Å] and angles [°].

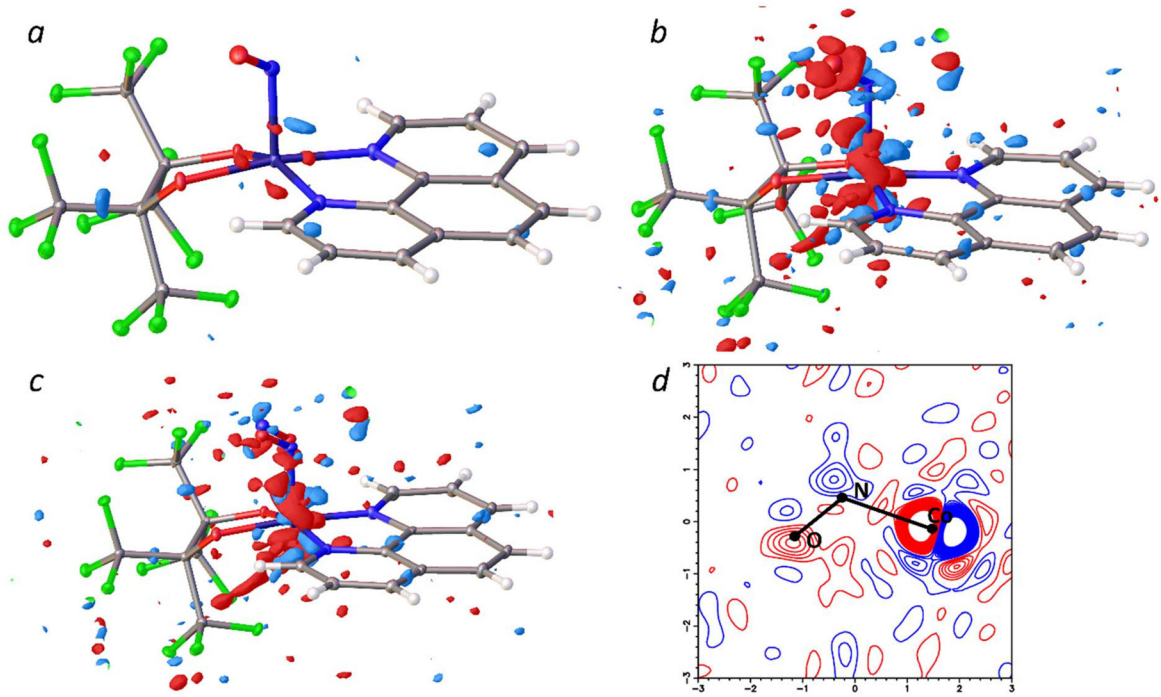

Fig. 3 Residual density maps of (a) the GS model applied to the structural dataset before irradiation, (b) the GS (Co–N–O) model applied to the dataset after irradiation, and (c) the disordered GS/PLI (Co–N–O/Co–O–N) model with 76(2)% population of the PLI applied to the dataset collected after irradiation; (d) photodifference (PD) map of the PLI and GS. The contour level for the residual density maps is 0.65 e Å^{-3} and for the PD map, it is 0.5 e Å^{-3}. The red areas correspond to the negative electron density (lack of electron density) and the blue areas correspond to positive electron densities (excess of electron density).

density map shown in Fig. 3a (the GS model applied to the dataset of the non-irradiated crystal) does not show any significant feature, confirming that the structural model perfectly fits the experimental electron density of the GS. Then, the same model with the GS configuration of Co–N–O has been applied to the dataset after irradiation (Fig. 3b). In the residual density map of this model, there are several significant residuals: negative electron density on the O atom (red, overestimation of electron density at this position) and positive electron density on the N atom of NO (blue, underestimation of electron density at this position). These two features are strong indicators of an interchange of the position of N and O in the PLI, since the difference of one electron between these two atoms leads to an over- or under-estimation of the actually present electron density at each position.[28] Finally, the disordered GS/PLI model with occupations of 0.24(2)/0.76(2) applied to the irradiated sample exhibits significantly reduced residual densities at the NO position, yielding a satisfactory description of the electron density (see Fig. 3c). The remaining residual electron density on the central Co reflects a small Co displacement after NO isomerization. With 24(2)% of NO in the GS and 76(2)% of ON in the PLI, we refine a single average position for Co without disorder, which results in the observed residual electron density around Co.[29] Further evidence for the modelled isonitrosyl configuration comes from the model-free analysis of photo-induced changes using so-called photodifference (PD) maps.[30] Similar to residual electron density maps, PD maps show increase (blue contours) or decrease (red contours) of electron density in PLI compared to GS, but based on the difference of the experimental structure factors of the irradiated and non-irradiated samples (F_{PLI}^{obs}–F_{GS}^{obs}, see Fig. 3d). In the present case, the PD map shows a significant increase in electron density at the N_{NO} position and a corresponding decrease in electron density at O_{NO} after irradiation, strongly supporting the NO rotation by 180° after excitation.

Chosen bond distances and angles of GS and PLI as well as the corresponding differences Δ(PLI–GS) are presented in Table 1, together with the results of the DFT geometry optimization. For the following discussion, we have to keep in mind that the distances and angles from the experiment are affected by the fact that we model only a single Co atom on an average position for the GS and PLI, and that we have closely overlaying Co–N–O and Co–O–N structures with different populations.

In the PLI, the volume of the unit cell increases by 0.97%, whereby the lattice constants increase and the triclinic angles decrease. The measured N1–O1/O1A–N1A distances in the GS and PLI are the same within 0.002 Å, but the DFT data show a shortening by 0.0114 Å. The Co1–O1A–N1A angle is slightly larger in the PLI (by 1.11°), so that the Co1–N1–O1 and Co–O1A–N1A structures are nearly the same in the GS and PLI, except that the NO ligand is rotated by 180° in the PLI and the

Co–O1A distance is 0.156 Å longer compared to Co1–N1. There is a small change in the position of the Co1 atom in the PLI with respect to the basal plane. The N2–Co1–O3 and N3–Co1–O2 angles increase by 2.58° and 5.17°, respectively, so that Co1 moves toward the basal plane. Additionally, the C1–C4 distance in the fpin is by 0.011 Å longer in the PLI, illustrating the effect of the isomerization on the other ligands.

The measured distances and angles in the GS match quite good with the calculated ones. We have performed two different DFT calculations (see the SI for details): CASTEP for the solid state (Table 1) and ADF for the molecule in the gas phase (Table S2). They match with each other in the second digit for the distances and differ by some degrees for the angles. Interestingly, the calculated N–O distances decrease in the PLI by 0.0114 Å (CASTEP) and by 0.0129 Å (ADF), so that this shortening seems to be a real feature of the PLI. The calculated (CASTEP) Co1–N1 distance is by 0.0691 Å shorter compared to the experiment. In the PLI, the calculated Co1–O1A and Co–N1A distances are by 0.1001 Å and 0.0454 Å shorter compared to the experiment. The differences of all other distances are in the second digit. The calculated (CASTEP) Co1–O1A–N1A angle is by 3.59° larger than the measured one. All other angles of the PLI agree within 10°. Given that the population of the PLI is not 100% and that the structure factor depends linearly on the population so that the experimental error is significantly larger than the statistical error, we consider the observed agreement between the experimental and calculated data as very good.

Photoswitching mechanism

Vibrational spectroscopy is a very sensitive method for the detection of structural rearrangements after light irradiation, since it allows for the measurement of relatively weak signals and tiny shifts of the vibrations of the relevant atomic groups. For the detection of nitrosyl linkage isomers, the (NO) stretching vibration can serve as a fingerprint.[31] In combination with UV/Vis spectroscopy, one can get valuable insight into the photoswitching mechanism, even under static measurement conditions.[32] Fig. 4a shows the observed changes upon irradiation; the band area of the $\tilde{\nu}$(NO) stretching vibration of the GS at 1708 cm^{-1} decreases and the new band of the PLI arises at 1780 cm^{-1}. From the reduction of the $\tilde{\nu}(NO)_{GS}$ band area, the population of the GS and thus the PLI can be calculated using the formula: $P_{PLI} = (1 - A_{irr}/A_0) \times 100\%$, where A_0 and A_{irr} are the area before and after irradiation, respectively. The position of the $\tilde{\nu}(NO)_{PLI}$ stretching vibration increases by 72 cm^{-1} (blue-shift) from 1708 cm^{-1} to 1780 cm^{-1} upon a PLI population of 79(3)% by irradiation with 590 nm light. The CASTEP calculations give a blue-shift of 18 cm^{-1} from 1647 cm^{-1} in the GS to 1665 cm^{-1} in the PLI. The difference between measured and calculated data is quite large: 62 cm^{-1} for the GS and 116 cm^{-1} for the PLI. The measured area of $\tilde{\nu}(NO)_{PLI}$ in the PLI is by a factor of 8.8 smaller compared to that of the GS, so that the derivative of the dipole moment is much smaller (by a factor of about 2.5) in the PLI. This points to a new arrangement of the charges on N and O, since the N–O distance does not change significantly. The first overtone of $\tilde{\nu}(NO)_{GS}$ is detected at 3387 cm^{-1}, which is by 29 cm^{-1} lower compared to the ideal harmonic overtone at 3416 cm^{-1}, so that the potential of the $\tilde{\nu}$(NO) vibration in the GS is anharmonic. Remarkably, as shown in Fig. 4b, the $\tilde{\nu}(NO)_{PLI}$ absorption band shifts to higher wavenumbers as a function of population from 1777 cm^{-1} to 1780 cm^{-1} by 3 cm^{-1} (measured with a resolution of 1 cm^{-1}), whereby the band of the GS remains at 1708 cm^{-1}, indicating that this effect concerns only the PLI species. Due to the fact that the low-frequency modes are strongly coupled between each other, the $\tilde{\nu}$(CoN) and δ(CoNO) vibrations cannot be unambiguously assigned. The two bands at 531 cm^{-1} and 458 cm^{-1} might correspond to these modes, since they disappear upon PLI generation, but there is no clear evidence for new increasing bands. Most of the vibrational bands shift by 1–3 cm^{-1} to higher or lower wavenumbers upon PLI generation (see SI, Fig. S1), witnessing a small effect of the NO rotation on nearly all atoms. From the CASTEP calcu-

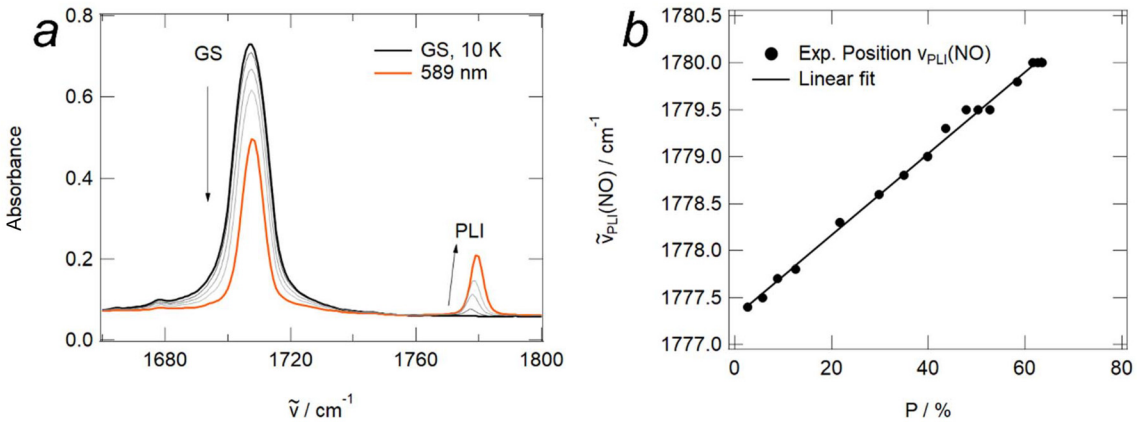

Fig. 4 (a) Infrared spectra in the range of 1800–1660 cm^{-1} at 10 K for the GS (black line) and different PLI populations (8, 20, 33, 56%) after 589 nm irradiation (grey and red lines). The experimental resolution is 2 cm^{-1}. (b) Shift of the $\tilde{\nu}(NO)_{PLI}$ position of the NO stretching vibration in PLI as a function of the PLI population measured with an experimental resolution of 1 cm^{-1}.

lations, we find δ(CoNO) = 672 cm^{-1} and $\tilde{\nu}$(CoN) = 375 cm^{-1} for the GS and δ(CoON) = 482 cm^{-1} and $\tilde{\nu}$(CoO) = 339 cm^{-1} for the PLI, and thus a downshift of 190 and 36 cm^{-1}, respectively.

Overall, the experiment and calculation show that in the PLI, the $\tilde{\nu}(NO)_{PLI}$ stretching vibration shifts to higher wavenumbers, while the $\tilde{\nu}$(CoO) and δ(CoON) vibrations shift to lower wavenumbers. These results are in qualitative agreement with earlier observations made for {PtNO}^{8} complexes.[17,18] For $[Pt(NH_3)_4Cl(NO)]Cl_2$, formally {Pt(II)NO$^+$} with 5d^8 d-orbital population,[18] the $\tilde{\nu}$(NO) stretching vibration shifts also to higher wavenumbers (+120 cm^{-1}), the $\tilde{\nu}$(Pt–N/O) and δ(PtNO) shift to lower wavenumbers, and the calculated N–O distance decreases by 0.0238 Å. The Pt–N–O angle is 117.5° in the GS and the Pt–O–N angle is 127.2° in the PLI. The difference to the Co complex is that the rotated ON_{PLI} is not overlapped with the position of NO_{GS}, but the ON is on the opposite site of the NO.[18]

Based on the knowledge of the structure and spectral fingerprints, we can now investigate the photoswitching mechanism, in order to describe it in a simplified potential scheme.

First, in order to get insight into the stability of the PLI, we determined the activation energy E_A of the PLI, which gives the energy difference between the PLI minimum and the crossing point of both GS and PLI potentials. For this, we measured the time-dependent increase in the area of $\tilde{\nu}(NO)_{GS}$ and decrease in the area of $\tilde{\nu}(NO)_{PLI}$ at different temperatures. From the resulting Arrhenius plot (see Fig. S2), we obtain the activation energy E_A = 0.104(2) eV and the frequency factor lg k_0 = 6.0(2). This very low activation energy might explain the decay of the PLI induced by the irradiation with the infrared light of the IR-spectrometer (see the discussion below).

Second, we analyse the photoswitching efficiencies for GS to PLI and PLI to GS conversion. In order to demonstrate that the PLI population depends only on the number and energy of the exciting photons, we measured the dependence of the PLI population on the excitation wavelength (see Fig. S3) and the energy flux Q (product of intensity and time). We used an OPO laser with a band width of 2 nm and a pulse duration of 5 × 10^{-9} s, as well as various cw-lasers and LEDs, reaching a maximum of the PLI population of 79(3)% under irradiation at 606 nm. Notably, irradiation with cw-light and ns-pulse-light results in the same PLI population behaviour with respect to dynamics and saturation. The PLI population dynamics *vs.* the energy flux Q shown in Fig. 5 follows an exponential increase, $P(Q) = P_\infty(1 - \exp(-Q/Q_0))$, where Q is the energy flux in J cm^{-2}. The 1/*e*-value is reached at Q_0 = 2.2(2) J cm^{-2}, corresponding to 6.5 × 10^{18} photons per cm^2 at the excitation wavelength λ_{exc} = 590 nm. At about 6 J cm^{-2}, the PLI population reaches saturation, *i.e.*, the saturation is reached in about 7 min at a relatively low intensity of 15 mW cm^{-2} (λ_{exc} = 590 nm). The back-transfer to the GS can be performed at 1050 nm (Fig. 5) and is more efficient than the PLI generation. At 1050 nm, the 1/*e*-value is reached at Q_0 = 0.16(2) J cm^{-2}, corresponding to 8.4 × 10^{17} photons per cm^2, and hence 0.5 J cm^{-2} are sufficient to completely depopulate the PLI. When comparing with the 9.6 × 10^{17} molecules present in our sample (m = 0.96 mg) and the area of the KBr pellet used for IR spectroscopy (1.326 cm^2), we thus obtain Q_0 values of 9 and 1.2 photons per molecule for the population at 590 nm and the depopulation at 1050 nm. From Fig. 5, we see that at Q_0, we have transferred approximately 50% of all molecules into the other state, so that we obtain rather high switching probabilities of approximately 5% for the GS-to-PLI transformation and 40% for the PLI-to-GS transformation, without considering the effective absorption.

As can be seen from Fig. S3, the GS to PLI conversion is most efficient for 606 nm and drops to zero when using light below 500 nm or above 800 nm. As a matter of fact, we also noted a depopulation of the PLI by the infrared probing beam of the spectrometer. This depopulation is quite fast, and after a few minutes in the beam of the spectrometer, the PLI is completely transferred back to the GS. We then obtained the UV/Vis absorption spectra of two samples with different concentrations of (**1**) to cover the spectral range from 3.5 to 0.7 eV

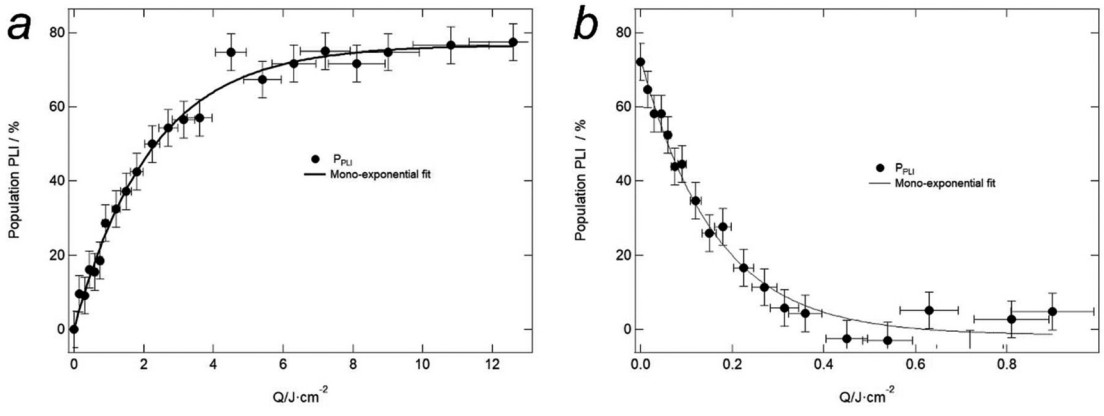

Fig. 5 PLI population as a function of energy flux Q. (a) During population of the PLI at 590 nm, the mono-exponential fit for $P(Q)$ yields Q_0 = 2.2(2) J cm^{-2} and P_∞ = 77(3)%; (b) during depopulation of the PLI at 1050 nm, the mono-exponential fit for $P(Q)$ yields Q_0 = 0.16(2) J cm^{-2} and P_∞ = −2 (3)%.

(350–1800 nm) to determine the involved electronic transitions. Experimentally, we find the two lowest transitions of the GS at 1.99 and 2.12 eV corresponding to 623 and 585 nm (see Fig. S4). Upon PLI generation, a weak broad band arises at 1.13 eV (1100 nm, see Fig. S5 for the fit of this band whose tail extends far into the infrared region, down to nearly 0.5 eV) and two strong bands at 2.53 and 2.77 eV (490 and 448 nm) with a third band at around 3.0 eV visible as a shoulder in the difference spectra. This clearly explains the PLI population window between 500 and 800 nm with a maximum at 606 nm, a simple result of the photostationary equilibrium between the GS to PLI and PLI to GS conversion for each given wavelength. Taking into account the absorption values for 590 nm and 1050 nm, we can calculate the quantum efficiencies for the photoswitching (see the SI for details on calculation), we obtain 0.10(1) and 1.07(19) for population and depopulation, respectively. The assignment of the observed absorption bands can be made using DFT and TD-DFT calculations (see the SI for details). As a result, we find that for both the GS and the PLI, the low-lying observed transitions correspond to metal-to ligand charge transfer transitions (MLCTs). Therefore, the photoswitching is triggered through the weakening of the metal–NO bond and (transient) occupation of anti-bonding ligand orbitals, as known from other nitrosyl compounds.[15] This interpretation is confirmed by X-ray absorption spectroscopy (XAS) measurements under light irradiation and the corresponding TD-DFT calculations (see the SI for details, Fig. S6 and S7), which can be used to analyse the origin of the pre-edge peak and its light-induced changes.[33] These calculations also point to a significant increase in the contribution of the NO orbitals in the LUMO of the PLI and a corresponding decrease in Co and other ligand contributions, which explains the observed lower intensity of the pre-edge peak. This increase in NO contribution to the LUMO might be at the origin of the observed high quantum yield for the PLI-to-GS photoswitching.

Concerning the depopulation by the infrared beam of the spectrometer, we performed further IR measurements by selectively blocking the emission of the IR source (from 50 to 12 000 cm^{-1}) with appropriate filters (InSb, Ge, polyethylene). As a result, we find that the PLI is stable if blocking the IR-light above 1400 cm^{-1} using a 0.1 mm thick InSb filter (direct bandgap of 0.17 eV).[34] The depopulation is significantly slowed down when inserting a 0.5 mm thick polyethylene filter, which blocks the light from 1400 cm^{-1} to 12 000 cm^{-1} partially, especially in the ranges of 1260–1520 cm^{-1} and 2240–12 000 cm^{-1}.[35] Finally, when using a 3 mm thick Ge filter (bandgap of 0.66 eV, 5300 cm^{-1}),[36] we observe a depopulation, which is only slightly slower than without this filter. This indicates a depopulation pathway through excitation into the broad absorption band with the maximum at 1100 nm, corresponding to the MLCT transition.

From this systematic study of the population and depopulation of the PLI, we can draw the potential scheme shown in Fig. 6, where the two potentials correspond to the GS and PLI structures. A particular feature of this cobalt nitrosyl compound is low-lying transitions in the PLI, enabling a back transfer to the GS in the far infrared spectral range. In all other aspects, the photoswitching mechanism corresponds to that known from {MNO}^{6} compounds. Starting from the GS, the PLI can be populated using wavelengths between 500 and 800 nm through an excitation into GS* followed by an internal conversion (IC) towards PLI* and subsequent vibrational relaxation into the PLI. The population window is defined by the equilibrium between these forward processes and the corresponding more efficient backward (PLI to GS) processes induced by excitation at wavelengths below 800 nm (up to almost 2500 nm) and above 500 nm. The activation barrier of the PLI is 0.1 eV, which is very small.

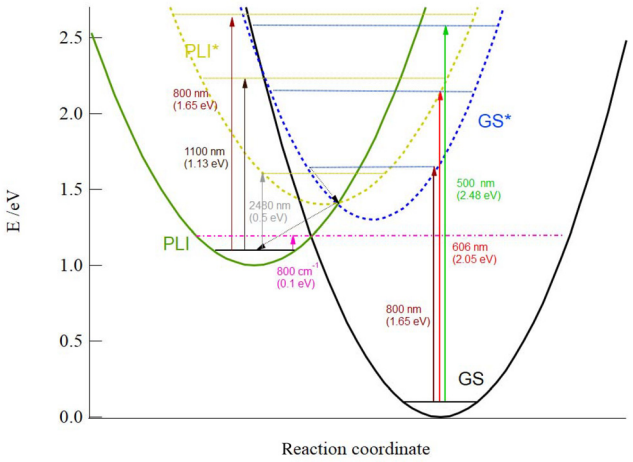

Fig. 6 Potential scheme summarising the photoswitching mechanism in (**1**).

In the PLI, the electronic structure and the bonding properties are changed. The Co–O–N structure is concomitant with a new organisation of the electron density, so that the energetic positions of the orbitals are shifted and/or rearranged (as seen from the UV/Vis measurements and TD-DFT calculations). In order to characterise [Co(fpin)NO(phen)] as a {CoNO}^{8} complex with formal charges {Co(I)NO^+} and $3d^8$ d-orbital population, we have measured its magnetic properties before and after irradiation. Characteristic magnetisation curves are presented in the SI (Fig. S8 and S9). In the GS, the sample is diamagnetic and in the PLI, the diamagnetism is only marginally increased; thus, there is no magnetic phase transition induced by light. Consequently, no free spin exists in the GS and PLI, which underlines the formally {Co(I)NO^+} with $3d^8$ d-orbital population for the GS and PLI and only one d-orbital is unoccupied.

Local modes and charge distribution

Together with the earlier reported {PtNO}^{8} and {RhNO}^{8} complexes,[17–19] we have now with {CoNO}^{8}, a third example of {MNO}^{8} compounds exhibiting the PLI. In all of them, the NO stretching frequency exhibits a blue-shift in the range of 70–130 cm^{-1} for the PLI compared to the GS, even though the

structures and structural changes are significantly different for the three examples. Following our recent report,[16] we will analyse the coupling between the different atomic movements, in order to try to interpret thoroughly the observed shifts of the vibrational modes. Therefore, we have calculated the decoupled vibrations and the corresponding local force constants using the Cremer–Kraka formalism.[27] The results are presented in Table 2, together with the calculated bond lengths. In the GS, the decoupled $\tilde{\nu}$(N–O) vibration shifts to lower wavenumbers by 19 cm^{-1}, but the $\tilde{\nu}$(Co–N) shifts to higher wavenumbers by 297 cm^{-1} compared to the coupled ones, indicating a weak coupling of NO and a strong coupling of Co–N. In the PLI, however, the coupling of Co–O is significantly weaker, resulting in a blue-shift of only 50 cm^{-1}, and the coupling of the $\tilde{\nu}$(O–N) gives a red-shift of 34 cm^{-1}. Hence, the movements of $\tilde{\nu}$(Co–O) and $\tilde{\nu}$(O–N) in the PLI are nearly independent from each other. They can be considered as quasi-free harmonic oscillators. It is instructive to compare these results with those obtained for $K_2[RuCl_5NO]$[16] (see below for more details), in which the GS κN nitrosyl Ru–N–O and the PLI κO isonitrosyl Ru–O–N are linear. In the {RuNO}^{6} complex, the $\tilde{\nu}$(Ru–N) and the $\tilde{\nu}$(N–O) have a blue-shift of 243 cm^{-1} and a red-shift of 70 cm^{-1}, respectively, upon decoupling in the GS. In the PLI, there is a blue-shift of 161 cm^{-1} for $\tilde{\nu}$(Ru–O) and a red shift of 31 cm^{-1} for $\tilde{\nu}$(O–N) upon decoupling. Hence, in the ruthenium complex with the linear NO group, due to the remaining strong $\tilde{\nu}$(Ru–O), we cannot consider them as quasi-free harmonic oscillators.

Knowing the effect of the coupling on the vibrational frequencies in the GS and PLI, we can now have a look at the charge distribution in the CoNO group in the GS and PLI, in order to interpret the positive shift of the $\tilde{\nu}$(N–O) stretching vibration. The results of DFT (CASTEP) calculations on the periodic crystalline systems are presented in Table 3, in terms of Bader charges on the atoms and the corresponding volumes of the Bader basins.[37] The CoNO group becomes by 0.10|e| more positive in the PLI (+1.07|e|) compared to that in the GS (+0.97|e|). The detailed analysis shows that the charges on cobalt and oxygen are changed only marginally by +0.01|e| and −0.01|e|, respectively. The major effect stems from the nitrogen, which increases by 0.10|e| from +0.16 to +0.26, so that NO becomes by +0.09|e| more positive in the PLI, but in absolute terms still remains slightly negative (−0.12|e|). The corresponding electronic charge of −0.09|e| is distributed over the atoms of other ligands (see Table 3), where the decrease on N3–C16 of phen (−0.07|e|) and O3 of fpin (−0.03|e|) is the most prominent. The rearrangement of the charges is connected with the change of charge volumes on the atoms. Keeping in mind that N1 and O1 (of NO) merely interchange their positions, the observation that the Bader volume of N1 increases from 88.87 to 130.34 Å^3 (+31.8%), while that of O1 decreases from 122.29 to 93.82 Å^3 (−23.3%) is not surprising. Note that the volume in the PLI of the now peripheral N1 is 6.2% larger compared to the peripheral O1 in the GS. Overall, the Bader volume of N1O1 increases by 5.8% in the PLI, so that the lower number of electrons on the NO is distributed in a larger volume, resulting in a net reduction by nearly a factor of 2 of the electronic charge per Å^3. All in all, the increased volume of Co–O–N by 16.22 Å^3 is a clear hint toward the reduced interaction energy in the PLI, which is consistent with a higher energetic position of its potential minimum with respect to the GS (Fig. 6).

If we summarise our findings from the calculations, using the decoupled parameters and the corresponding charge distribution (see Table 4), we find that when going from the GS to the PLI: (1) the decoupled $\tilde{\nu}$(N–O) vibration shifts by only 3 cm^{-1} to higher wavenumbers (from 1628 to 1631 cm^{-1}); (2) the decoupled force constant correspondingly also increases slightly by 0.045 N cm^{-1} (from 11.658 to 11.703 N cm^{-1}); (3)

Table 3 DFT calculated Bader charges (electron charge, e) and Bader volumes [Å^3] for Co–N–O and other chosen atoms in the crystalline systems

	Bader charges (|e|)			Bader volumes (Å^3)		
Group	GS	PLI	Δ(PLI–GS)	V(GS)	V(PLI)	ΔV(PLI–GS)
Co	+1.18	+1.19	+0.01	62.06	65.28	+3.22
N1	+0.16	+0.26	+0.10	88.87	130.34	+41.47
O1	−0.37	−0.38	−0.01	122.29	93.82	−28.47
N–O	−0.21	−0.12	+0.09	211.16	224.16	+13.0
Co–N–O	+0.97	+1.07	+0.10	273.22	289.44	+16.22
N2	−1.13	−1.15	−0.02	78.15	80.69	+2.54
N3	−1.13	−1.12	+0.01	84.10	83.30	−0.80
O2	−1.01	−1.00	+0.01	95.68	96.44	+0.76
O3	−1.01	−1.04	−0.03	85.25	86.38	+1.13
O2–C1	+0.58	+0.59	+0.01	37.75	37.61	−0.14
O3–C4	+0.63	+0.66	+0.03	37.12	36.64	−0.48
N2–C7	+0.54	+0.53	−0.01	66.88	72.41	+5.53
N2–C18	+0.43	+0.43	±0.00	55.20	54.00	−1.22
N3–C17	+0.43	+0.45	+0.02	56.11	53.68	−2.43
N3–C16	+0.55	+0.48	−0.07	74.37	75.39	+1.02
C1–C2	+0.58	+0.59	+0.01	22.57	22.84	+0.27
C4–C5	+0.63	+0.66	+0.03	22.79	22.71	−0.08
C18–C10	+0.43	+0.43	±0.00	64.29	64.01	−0.28
C17–C13	+0.43	+0.45	+0.02	68.18	67.34	−0.84

Table 2 Calculated bond lengths, force constants and wavenumbers with the differences between decoupled and coupled vibrations

			Force constant (N cm^{-1})			Wavenumber (cm^{-1})		
	$\tilde{\nu}$ mode	Bond length (Å)	Decoupled	Coupled	Δ	Decoupled	Coupled	Δ
GS	N–O	1.1822	11.658	11.932	−0.274	1628	1647	−19
	Co–N	1.7608	3.012	0.938	2.074	672	375	297
PLI	O–N	1.1708	11.703	12.196	−0.493	1631	1665	−34
	Co–O	1.8859	1.121	0.851	0.270	389	339	50

Table 4 Comparison of the decoupled stretching vibrations, local force constants, Bader charges, and N–O distances of GS and MS1 in $K_2[RuCl_5NO]$ with GS and PLI in [Co(fpin)(NO)(phen)]

	$K_2[RuCl_5NO]$ (from ref. 16)			[Co(fpin)(NO)(phen)]		
	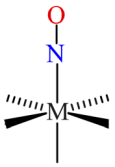	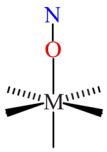	Δ	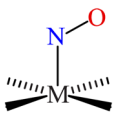	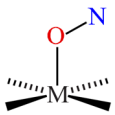	Δ
$\tilde{\nu}$(N–O), cm^{-1}	1799	1741	−58	1628	1631	3
k(N–O), N cm^{-1}	14.239	13.334	−0.905	11.658	11.703	0.045
q(NO), e	−0.15	−0.08	0.07	−0.21	−0.12	0.09
d(N–O), Å	1.152	1.154	0.002	1.1822	1.1708	−0.0104
M–N–O, °	172.5	172.8	0.3	124.4	126.7	2.3

the NO ligand becomes by +0.09|e| more positive in the PLI (from −0.21|e| to −0.12|e|). These findings are consistent with the slight decrease in the CASTEP calculated NO distance by −0.0144 Å in the PLI, in the sense that an increase in the frequency of the NO stretching vibration is correlated to a more positive NO and a shorter NO distance. Qualitatively, in this specific case, even the calculated coupled (and experimental) results show the same behaviour, *i.e.*, an increase in the NO stretching frequency in the PLI. However, we can see that there is a significant quantitative difference between the experimental shift and the decoupled one, so one would probably largely overestimate the expected change in NO charge and distance if one would try to infer it from the experimental value of the shift of the NO stretching frequency.

When comparing the Co–N–O angle of 124.4° in the GS with the Co–O–N angle of 126.7° in the PLI, we note a small increase of 2.3°, so we might consider the PLI of [Co(fpin)(NO)(phen)] as an isonitrosyl configuration, *i.e.*, a 180° rotation of the NO ligand. We can thus recall the case of $K_2[RuCl_5NO]$, a $\{MNO\}^6$ compound which we analysed recently in the same manner.[16] This ruthenium nitrosyl complex presents a PLI corresponding to an isonitrosyl configuration (MS1 state), but showing a linear Ru–N–O configuration with a Ru–N–O angle of 172.5° in the GS and a Ru–O–N angle of 172.8° in the PLI. For $K_2[RuCl_5NO]$, we observe the following changes (using the calculated decoupled values, see Table 4) upon PLI generation: (1) the $\tilde{\nu}$(N–O) vibration shifts by 58 cm^{-1} to lower wavenumbers (from 1799 to 1741 cm^{-1}); (2) the force constant correspondingly also decreases by 0.905 N cm^{-1} (from 14.239 to 13.334 N cm^{-1}); (3) the NO ligand becomes by 0.07|e| more positive in the PLI (from −0.15|e| to −0.08|e|); (4) the NO distance increases marginally by 0.002 Å (from 1.152 to 1.154 Å). Thus, in this case, the decrease in the frequency of the NO stretching vibration is correlated to a more positive NO and a slightly longer NO distance. We observe thus in both cases, $\{MNO\}^8$ and $\{MNO\}^6$, a more positive NO in the isonitrosyl configuration, but this leads to a (tiny) blue-shift of the NO stretching frequency in the case of the $\{MNO\}^8$ cobalt complex, while it leads to a comparatively larger red-shift in the case of the $\{MNO\}^6$ ruthenium complex. Clearly, the different bonding situations (linear *vs.* bent) in the two compounds affect both the coupling strength of NO to M–N/O as well as the vibrational changes upon isomerisation. In the linear configuration, the M–O and O–N groups cannot move independently. Another important difference between $\{MNO\}^6$ and $\{MNO\}^8$ is the difference in the d-orbital positions and populations,[21] whereby the energetic positions of the empty π* orbitals of NO in diamagnetic d^8 compounds lie above the occupied metal $d(z^2)$ orbital, which forms a sigma bond with the π*(yz) of NO. This bond is responsible for the bent M–N–O geometry in the GS and PLI. In $\{MNO\}^6$ complexes, the isonitrosyl MS1 is reached by a two-step process GS → MS2 → MS1.[12] MS2 states (κ^2N,O-geometry) do not exist in diamagnetic $\{MNO\}^8$ complexes, so that the PLI (corresponding to an isonitrosyl configuration, similar to MS1) is reached by a full N–O rotation as found in the diamagnetic Co($3d^8$), Rh($4d^8$), and Pt($5d^8$). The generation of linkage isomers in both cases is the same in the orbital picture: the necessary condition is a MLCT transition from the occupied d-orbitals to the empty antibonding orbitals of π*(NO), followed by a relaxation into the energetic minimum of the PLI, as shown in Fig. 6. The rotation of N–O starts most probably due to the occupation of an excited vibrational–rotational state during the initial excitation, whereby the M–N bond strength is reduced by the occupation of the antibonding π*(NO) orbital. This then results in an internal conversion and the radiationless transition from the exited GS to the PLI minimum.

Conclusion

We have determined the structure and properties of one PLI in a diamagnetic $\{CoNO\}^8$ complex. It corresponds to a nearly 180° rotation of the NO ligand, so that both the GS and the PLI are bent metal-nitrosyl configurations. The photoswitching from the GS to the PLI is highly efficient, 80% of the PLI can be generated by irradiation at 606 nm and a quantum efficiency of 0.1. The complete reversal from the PLI to the GS can be induced by infrared light with a quantum efficiency of 1. The photoswitching mechanism is the same as that found

in $\{MNO\}^6$ complexes; the forward and backward conversion between the GS and PLI is triggered by a MLCT transition ($d(Co) \rightarrow \pi^*(NO)$), resulting in a weakening of the NO bond allowing for the rotation of NO before relaxing into the metastable minimum of the PLI. There is only one PLI for the bent $\{CoNO\}^8$, which however resembles the isonitrosyl PLI of the linear $\{MNO\}^6$ insofar as it corresponds to a 180° rotation of NO. All these characteristic features are present in the electron-rich diamagnetic bent Co($3d^8$)-, Rh($4d^8$)- and Pt($5d^8$)-nitrosyl complexes, so that in general the occupied d(z^2)-orbital, which forms a σ-bond with one of the anti-bonding π* (NO)-orbitals, is responsible for the bent M–N–O angle and especially for the existence of a single photoinduced linkage isomer. Even though the photoswitching mechanism is the same as for the $\{MNO\}^6$ complexes, there are some distinct differences, which confirm previous results obtained for $\{PtNO\}^8$ and $\{RhNO\}^8$ complexes: the energies needed for the photoswitching are much lower in the red spectral range (around 600 nm) for the GS to PLI conversion and in the infrared spectral range (1100 nm) for the PLI to GS conversion. We note that especially the back conversion is possible with light of energy down to 0.5 eV, and moreover that the switching efficiency is very high. The local mode analysis also shows different results for the $\{MNO\}^8$ complexes compared to their $\{MNO\}^6$ counterparts; although in the isonitrosyl PLI in both cases, the NO ligand gets more positive charge, it results in opposite shifts of the NO stretching vibration, a blue-shift for the $\{MNO\}^8$ complexes and a red-shift for the $\{MNO\}^6$ complexes.

Author contributions

TW and DS conceived the work. AM, AH, SP, and DS performed photocrystallographic experiments and corresponding analysis. AM, TW, and DS performed spectroscopic (UV-Vis, IR) measurements and corresponding analysis. AG performed solid-state calculations and corresponding analysis. AM and GK performed gas-phase calculations, including TD-DFT, and kinetic analysis. AM and DS performed XAS measurements and analysis. AM, DS and GC performed magnetic and photomagnetic experiments. GC performed the analysis of magnetic data. AM, TW, and DS wrote the initial draft. All authors contributed to the writing of the final draft as well as to the discussion of the results.

Conflicts of interest

There are no conflicts to declare.

Data availability

The magnetic data supporting this article have been included as part of the supplementary information (SI). Supplementary information is available. See DOI: https://doi.org/10.1039/d6dt00116e.

Spectroscopic raw data (IR, UV-Vis, and X-ray absorption spectroscopy) and complete output files of calculations are available from the repository Recherche Data Gouv, under the link https://doi.org/10.57745/WA7RY3.

CCDC 2448993 and 2448997 for the GS and PLI contain the supplementary crystallographic data for this paper.[38a,b]

Acknowledgements

This work was financially supported by ANR (grant no. ANR-21-CE30-0045-01 and LUE-ANR-15-IDEX-04) and RSF (22-43-09001, https://rscf.ru/project/22-43-09001/). High performance computing resources were partially provided by the EXPLOR centre hosted by the Université de Lorraine. We thank the PMD2X platform of Université de Lorraine for granting access to XRD diffractometers. Beamtime at the LUCIA beamline of SOLEIL synchrotron (proposal 20221323) is gratefully acknowledged. A. H. thanks Région Grand Est for financial support (Project Number 19_GE6_108). We thank Tobias Riggenmann and Peter Klüfers from LMU Munich for providing the powder and single crystalline samples of (**1**). We further thank El-Eulmi Bendeif for help with low temperature X-ray diffraction experiments.

References

1 H. M. Elbeheiry and M. Schulz, *Coord. Chem. Rev.*, 2024, **515**, 215921.
2 P. K. Mascharak, *J. Inorg. Biochem.*, 2022, **231**, 111804.
3 G. R. Navale, S. Singh and K. Ghosh, *Coord. Chem. Rev.*, 2023, **481**, 215052.
4 D. Schaniel, M. Imlau, T. Weisemoeller, T. Woike, K. W. Krämer and H.-U. Güdel, *Adv. Mater.*, 2007, **19**, 723–726.
5 M. Goulkov, D. Schaniel and T. Woike, *J. Opt. Soc. Am. B*, 2010, **27**, 927.
6 D. Schaniel, J. Schefer, B. Delley, M. Imlau and T. Woike, *Phys. Rev. B: Condens. Matter Mater. Phys.*, 2002, **66**, 085103.
7 J. S. García, F. Alary, M. Boggio-Pasqua, I. M. Dixon and J.-L. Heully, *J. Mol. Model.*, 2016, **22**, 284.
8 I. Stepanenko, M. Zalibera, D. Schaniel, J. Telser and V. B. Arion, *Dalton Trans.*, 2022, **51**, 5367–5393.
9 J. M. Butler, M. W. George, J. R. Schoonover, D. M. Dattelbaum and T. J. Meyer, *Coord. Chem. Rev.*, 2007, **251**, 492–514.
10 M. S. Lynch, M. Cheng, B. E. Van Kuiken and M. Khalil, *J. Am. Chem. Soc.*, 2011, **133**, 5255–5262.
11 G. Gallé, M. Nicoul, T. Woike, D. Schaniel and E. Freysz, *Chem. Phys. Lett.*, 2012, **552**, 64–68.
12 A. Hasil, K. A. Konieczny, A. Mikhailov, S. Pillet and D. Schaniel, *ChemPhotoChem*, 2024, **8**, e202300149.

13 P. Coppens, I. Novozhilova and A. Kovalevsky, *Chem. Rev.*, 2002, **102**, 861–884.
14 T. E. Bitterwolf, *Coord. Chem. Rev.*, 2006, **250**, 1196–1207.
15 D. Schaniel and T. Woike, *Phys. Chem. Chem. Phys.*, 2009, **11**, 4391.
16 A. A. Mikhailov, A. Gansmüller, K. A. Konieczny, S. Pillet, G. Kostin, P. Klüfers, T. Woike and D. Schaniel, *Phys. Chem. Chem. Phys.*, 2024, **26**, 15255–15267.
17 D. Schaniel, T. Woike, N.-R. Behrnd, J. Hauser, K. W. Krämer, T. Todorova and B. Delley, *Inorg. Chem.*, 2009, **48**, 11399–11406.
18 D. Schaniel, T. Woike, B. Delley, D. Biner, K. W. Krämer and H.-U. Güdel, *Phys. Chem. Chem. Phys.*, 2007, **9**, 5149.
19 D. Schaniel, E.-E. Bendeif, T. Woike, H.-C. Böttcher and S. Pillet, *CrystEngComm*, 2018, **20**, 7100–7108.
20 J. Popp, T. Riggenmann, D. Schröder, T. Ampßler, P. Salvador and P. Klüfers, *Inorg. Chem.*, 2021, **60**, 15980–15996.
21 A. Hasil, D. Beck, D. Schröder, S. Pillet, E. Wenger, T. Woike, P. Klüfers and D. Schaniel, *Angew. Chem., Int. Ed.*, 2022, **61**, e202210671.
22 K. R. Sawyer, R. P. Steele, E. A. Glascoe, J. F. Cahoon, J. P. Schlegel, M. Head-Gordon and C. B. Harris, *J. Phys. Chem. A*, 2008, **112**, 8505–8514.
23 H. J. B. Marroux, B. F. E. Curchod, C. A. Faradji, T. A. Shuttleworth, H. A. Sparkes, P. G. Pringle and A. J. Orr-Ewing, *Angew. Chem., Int. Ed.*, 2017, **56**, 13713–13716.
24 S. Shin, J. Choe, Y. Park, D. Jeong, H. Song, Y. You, D. Seo and J. Cho, *Angew. Chem., Int. Ed.*, 2019, **58**, 10126–10131.
25 M. A. Rhine, A. V. Rodrigues, R. J. B. Urbauer, J. L. Urbauer, T. L. Stemmler and T. C. Harrop, *J. Am. Chem. Soc.*, 2014, **136**, 12560–12563.
26 M. R. Walter, S. P. Dzul, A. V. Rodrigues, T. L. Stemmler, J. Telser, J. Conradie, A. Ghosh and T. C. Harrop, *J. Am. Chem. Soc.*, 2016, **138**, 12459–12471.
27 Y. Tao, W. Zou, D. Sethio, N. Verma, Y. Qiu, C. Tian, D. Cremer and E. Kraka, *J. Chem. Theory Comput.*, 2019, **15**, 1761–1776.
28 B. Cormary, I. Malfant, M. Buron-Le Cointe, L. Toupet, B. Delley, D. Schaniel, N. Mockus, T. Woike, K. Fejfarová, V. Petříček and M. Dušek, *Acta Crystallogr., Sect. B:Struct. Sci.*, 2009, **65**, 612–623.
29 D. Schaniel, T. Woike, J. Schefer, V. Petříček, K. W. Krämer and H. U. Güdel, *Phys. Rev. B: Condens. Matter Mater. Phys.*, 2006, **73**, 174108.
30 S. Pillet, in *Structures on Different Time Scales*, ed. T. Woike and D. Schaniel De Gruyter, 2018, pp. 143–220.
31 A. A. Mikhailov, T. Woike, A. Gansmüller, D. Schaniel and G. A. Kostin, *Spectrochim. Acta, Part A*, 2021, **263**, 120217.
32 A. A. Mikhailov, A. T. Tiognou, A. O. Brovko, G. A. Kostin and D. Schaniel, *Dalton Trans.*, 2025, **54**, 8918–8931.
33 D. T. Kamgne, B. T. Sendja, D. O. De Souza, T. Woike, G. Aquilanti and D. Schaniel, *ChemPhotoChem*, 2022, **6**, e202200221.
34 C. L. Littler and D. G. Seiler, *Appl. Phys. Lett.*, 1985, **46**, 986–988.
35 J. V. Gulmine, P. R. Janissek, H. M. Heise and L. Akcelrud, *Polym. Test.*, 2002, **21**, 557–563.
36 P. J. Collings, *Am. J. Phys.*, 1980, **48**, 197–199.
37 R. F. W. Bader, *Chem. Rev.*, 1991, **91**, 893–928.
38 (*a*) CCDC 2448993: Experimental Crystal Structure Determination, 2026, DOI: 10.5517/ccdc.csd.cc2n6cs1; (*b*) CCDC 2448997: Experimental Crystal Structure Determination, 2026, DOI: 10.5517/ccdc.csd.cc2n6cx5.